Supplemental Material

Self oscillating synchronematic colloids

Sergi G. Leyva[1,2], Zhengyan Zhang[3], Monica Olvera de la Cruz [1,2,4], and Kyle J. M. Bishop[†3]

[1]Center for Computation and Theory of Soft Materials, Northwestern University, Evanston, IL, USA
[2]Department of Physics and Astronomy, Northwestern University, Evanston, IL, USA
[3]Department of Chemical Engineering, Columbia University, New York, NY, USA
[4]Department of Materials Science Engineering, Northwestern University, Evanston, IL, USA

---

m olvera@northwestern.edu
[†]kyle.bishop@columbia.edu

Contents

Supplemental Videos

Supplemental Video 1. Particle dynamics within a large fluid cluster, in which the particle density is approximately uniform throughout the imaging region (Figs. 1d and 2a). Video is acquired at 3000 frames per second (fps) and played back at 30 fps for a duration of 1000 frames (333 ms real time). The imaging region is 1280×800 px^2 = 1702×1064 μm^2 in size. Particles are annotated by colored ellipsoids that denote the oscillation phase and orientation.

Supplemental Video 2. Particle dynamics within three synchronematic crystals (Fig. 1e). Video is acquired at 3000 fps and played back at 30 fps for a duration of 400 frames (133 ms real time). The imaging region is 1280×800 px^2 = 1702×1064 μm^2 in size. The upper frame shows the raw images; the lower frame is annotated by colored ellipsoids that denote the oscilation phase and orientation.

Supplemental Video 3. Particle dynamics within a smaller fluid cluster, in which the particle density is varies across the imaging region (Figs. 2e,f). Video is acquired at 3000 fps and played back at 30 fps for a duration of 1000 frames (333 ms real time). The imaging region is 1280×800 px^2 = 1702×1064 μm^2 in size. Particles are annotated by colored ellipsoids that denote the oscillation phase and orientation.

Supplemental Video 4. Particle dynamics within a single synchronematic crystal containing $N \approx 110$ particles (Figs. 3a-c). Video is acquired at 3000 fps and played back at 15 fps for a duration of 400 frames (133 ms real time). The imaging region is 200×200 px^2 = 266×266 μm^2 in size. The images are annotated to show: (top, left) colored disks representing the hexatic order parameter ψ_6; (top, right) colored triangles indicating the instantaneous particle velocity $\mathbf{v}$; (lower, right) colored ellipsoids denoting the oscillation phase θ and orientation angle χ; (lower, left) colored disks representing the phase-angle order parameter $S_{\theta\chi}$ based on six nearest neighbors.

Supplemental Video 5. Simulated particle dynamics within a single synchronematic crystal containting $N = 70$ particles (Figs. 3d-f). The total simulation time is 44 ms. The images are annotated to show: (top, left) colored disks representing the hexatic order parameter ψ_6; (top, right) colored triangles indicating the instantaneous particle velocity $\mathbf{v}$; (lower, right) colored ellipsoids denoting the oscillation phase θ and orientation angle χ; (lower, left) colored disks representing the phase-angle order parameter $S_{\theta\chi}$ based on six nearest neighbors.

Supplemental Video 6. Transition from linear to circular synchronematic ordering extracted from experiments (Fig. 4a). Video is acquired at 3000 fps and played back at 15 fps for a duration of 720 frames (240 ms real time). The imaging region is 260×260 px^2 = 346×346 μm^2 in size. The images are annotated to show: (top, left) colored disks representing the hexatic order parameter ψ_6; (top, right) colored triangles indicating the instantaneous particle velocity $\mathbf{v}$; (lower, right) colored ellipsoids denoting the oscillation phase θ and orientation angle χ; (lower, left) colored disks representing the phase-angle order parameter $S_{\theta\chi}$ based on six nearest neighbors.

Supplemental Video 7. Transition from linear to circular synchronematic ordering extracted from simulations (Fig. 4b). The cluster contains $N = 70$ oscillators, and the video duration is 440 ms of simulated time. The images are annotated to show: (top, left) colored disks representing the hexatic order parameter ψ_6; (top, right) colored triangles indicating the instantaneous particle velocity $\mathbf{v}$; (lower, right) colored ellipsoids denoting the oscillation phase θ and synchronematic linear order; (lower, left) colored disks representing the linear nematic order parameter S_l based on six nearest neighbors.

Supplemental Video 8. Particle ejection and catastrophic disassembly of two synchronematic crystals (played sequentially). Video is acquired at 3000 fps and played back at 30 fps for a duration of 600 frames (200 ms real time). The imaging region is 200×200 px^2 = 346×266 μm^2 in size. Particles are annotated by colored triangles indicating the instantaneous particle velocity $\mathbf{v}$.

Supplemental Note 1: Analysis of oscillatory particle trajectories

Given tracking data for $k = 1, \ldots, N$ particle positions $\mathbf{y}_k$ at regular time intervals $t_k = k\Delta t$, we seek to determine latent (hidden) variables $\mathbf{s}_k$ that characterize the particle oscillator—namely, the oscillation phase θ_k, orientation angle χ_k, and position $\mathbf{x}_k$. To do so, we propose a generative, probabilistic model for the dynamics of an individual oscillator characterized by model parameters such as the oscillation frequency ω, phase diffusivity D_χ, angle diffusivity D_χ, etc. We use Bayesian inference to estimate both the latent variables and the model parameters from particle tracking data (Fig. S1). Below, we describe the model and outline the data analysis process; further details can be found in a forthcoming publication on characterizing "noise" in Quicke oscillators.

Generative Model

In the absence of noise, the transient position $\mathbf{y}(t)$ of an oscillating particle can be parameterized by the oscillator position $\mathbf{x}$, orientation χ, and phase $\theta(t)$ as

$$\mathbf{y}(t) = \mathbf{x} + \mathbf{n}(\chi) g(\theta(t)) \tag{1.1}$$

where $\mathbf{n}(\chi) = [\cos\chi, \sin\chi]^\top$ is a unit vector parallel to the oscillation direction, and $g(\theta)$ is the 2π-periodic waveform. By definition, the oscillation phase increases linearly with time as $\theta(t) = \omega t + \phi$, where ω is the oscillation frequency, and ϕ is the relative phase. Quincke oscillators are further distinguished by a symmetry whereby their dynamics is invariant to a simultaneous shift in phase $\theta \to \theta + \pi$ and angle $\chi \to \chi + \pi$.[1] This phase-angle symmetry implies the following constraint on the waveform: $g(\theta) = -g(\theta + \pi)$. We can therefore parameterize $g(\theta)$ by the Fourier series

$$g(\theta) = \sum_{n=1}^{\infty} b_n \cos[(2n-1)\theta] + c_n \sin[(2n-1)\theta] \tag{1.2}$$

where b_n and c_n are real-valued coefficients, collectively denoted $\mathbf{b}$. Without loss of generality, we set $c_1 = 0$, which determines the oscillation amplitude at zero phase, $\theta = 0$.

The noise-free oscillator is characterized by a constant position $\mathbf{x}$, orientation χ, and relative phase ϕ. In experiment, however, these variables are observed to change on time scales longer than the oscillation period $T = 2\pi/\omega$. We approximate these changes by a stochastic diffusion process parameterized by diffusion coefficients D_θ, D_χ, and D_x for the oscillator phase, angle, and position, respectively. Finally, to account for remaining discrepancies between the observed particle position and the predictions of equation (1.1), we model the measurement error by white Gaussian noise with zero mean and variance σ^2.

We denote the latent variables at time t_k by the state vector $\mathbf{s}_k = [\theta_k, \chi_k, x_{1k}, x_{2k}]^\top$. The joint distribution for the particle positions $\mathbf{y}_{1:N}$ and the latent variables $\mathbf{s}_{1:N}$ given the model parameters $\lambda = \{\omega, D_\theta, D_\chi, D_x, \mathbf{s}_0, \mathbf{b}, \sigma^2\}$ is

$$p(\mathbf{s}_{1:N}, \mathbf{y}_{1:N} \mid \lambda) = \prod_{k=1}^{N} p(\mathbf{s}_k \mid \mathbf{s}_{k-1}, \lambda) p(\mathbf{y}_k \mid \mathbf{s}_k, \lambda) \tag{1.3}$$

Here, the *process* model $p(\mathbf{s}_k \mid \mathbf{s}_{k-1}, \lambda)$ is a normal distribution with mean vector $\mathbf{s}_{k-1} + \mathbf{w}$ where $\mathbf{w} = [\omega\Delta t, 0, 0, 0]^\top$ and covariance matrix R_k given by

$$R_k = 2\Delta t \begin{bmatrix} D_\theta & 0 & 0 & 0 \\ 0 & D_\chi & 0 & 0 \\ 0 & 0 & D_x & 0 \\ 0 & 0 & 0 & D_x \end{bmatrix} \tag{1.4}$$

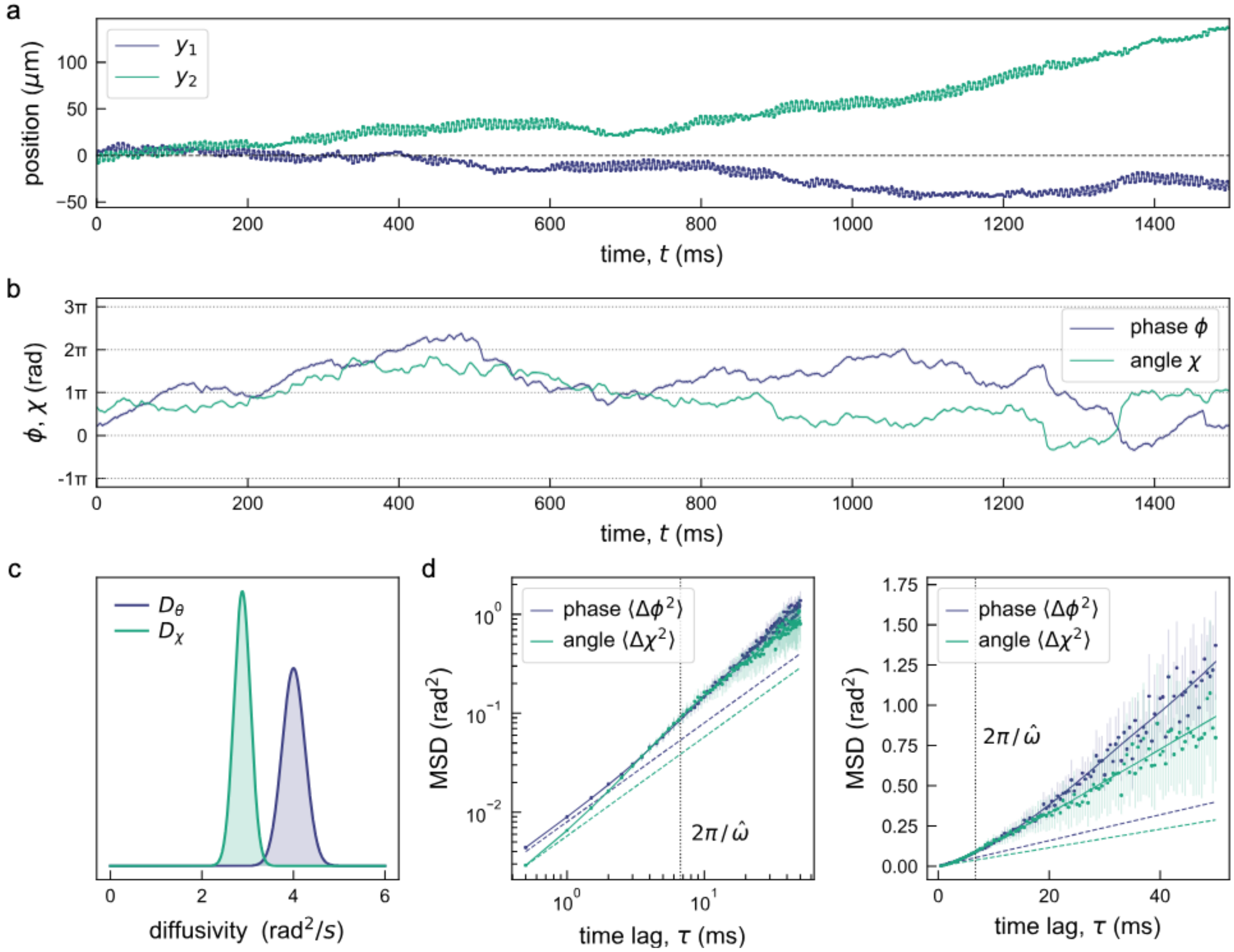

Figure S1: Analysis of an oscillatory particle trajectory. (a) Particle position $\mathbf{y}$ vs. time t at regular intervals of 0.5 ms from particle tracking (markers). The solid curve denotes the fitted trajectory based on the stochastic model described in the text. Particle radius is $a = 5$ μm; the AOT concentration is 150 mM; the external field strength is $E_{\mathrm{e}} = 6$ V/μm. (b) Inferred time-series of the relative phase $\phi = \theta \quad \hat{\omega} t$ and angle χ of the particle oscillator. The inferred frequency is $\omega = 938 \pm 6$ rad/s. (c) Approximate posterior distributions for the phase diffusivity D_θ and angle diffusivity D_χ. (d) Mean squared displacement (MSD) of the relative phase ϕ and angle χ as a function of time lag τ. Dashed lines denote the diffusive expectation $2D\tau$ for the inferred parameters $D_\theta = 4.0 \pm 0.25$ rad^2/s and $D_\chi = 2.9 \pm 0.18$ rad^2/s. Similar analysis of additional particles suggests an average frequency of $\omega = 1060 \pm 23$ rad/s, an average phase diffusivity of $D_\theta = 5.2 \pm 1.2$ rad^2/s, and an average angle diffusivity of $D_\chi = 4.3 \pm 0.6$ rad^2/s.

The oscillator phase, angle, and position change in time due to diffusion with coefficients D_θ, D_χ, and D_x. Furthermore, the phase θ_k increases with a constant drift velocity ω equal to the oscillation frequency. The *measurement* model $p(\mathbf{y}_k \mid \mathbf{s}_k, \lambda)$ is also normally distributed with mean vector

$$\mathbf{h}(\mathbf{s}_k) = \mathbf{x}_k + \mathbf{n}(\chi_k)g(\theta_k) \tag{1.5}$$

and covariance matrix $\sigma^2 I$, where I is the 2×2 identity matrix.

Parameter Estimation: Expectation-Maximization Algorithm

The posterior distribution for the latent variables $\mathbf{s}_{1:N}$ and the model parameters λ given the observed positions $\mathbf{y}_{1:N}$ is

$$p(\mathbf{s}_{1:N}, \lambda \mid \mathbf{y}_{1:N}) \propto p(\mathbf{s}_{1:N}, \mathbf{y}_{1:N} \mid \lambda)p(\lambda) \tag{1.6}$$

For simplicity, we assume a uniform prior for the parameters such that $p(\lambda) =$ constant over the range of interest. The distribution $p(\mathbf{s}_{1:N}, \mathbf{y}_{1:N} \mid \lambda)$ is described by equation (1.3). We use the expectation maximization algorithm[2] to identify the MAP estimates of the latent variables $\hat{\mathbf{s}}_{1:N}$ and the model parameters $\hat{\lambda}$ that maximize the posterior distribution of equation (1.6). In the j^{th} step of this iterative process, we evaluate the distribution $p(\mathbf{s}_{1:N} \mid \mathbf{y}_{1:N}, \lambda_j)$ for the latent variables conditioned on the observed positions and the current estimate of the model parameters. Using this distribution, we compute the expectation of the log likelihood $\ln p(\mathbf{s}_{1:N}, \mathbf{y}_{1:N} \mid \lambda)$ and maximize this function with respect to λ to obtain an improved estimate λ_{j+1}. Repeated iteration of the expectation and maximization steps converges to the desired MAP estimates.

Expectation Step: Kalman Filtering & Smoothing

We approximate the distribution $p(\mathbf{s}_{1:N} \mid \mathbf{y}_{1:N}, \lambda)$ using an extended Kalman filter with Rauch-Tung-Striebel smoothing.[2–4] This algorithm provides an efficient approach that scales linearly with the number of time steps N.

Forward Kalman Filter. During the first "filter" step, we progress through the unobserved states $\mathbf{s}_k$ from $k = 1$ to N conditioning on all observations up to and including $\mathbf{y}_k$. We denote the resulting distribution for $\mathbf{s}_k$ as $p(\mathbf{s}_k \mid \mathbf{y}_{1:k})$, where $\mathbf{y}_{1:k} = \{\mathbf{y}_1, \ldots, \mathbf{y}_k\}$. To streamline the notation, we have omitted the conditioning on the model parameters λ throughout this section. In progressing from index $k-1$ to k, we apply the following Bayesian updating procedure

$$p(\mathbf{s}_k \mid \mathbf{y}_{1:k}) \propto p(\mathbf{y}_k \mid \mathbf{s}_k)p(\mathbf{s}_k \mid \mathbf{s}_{k-1})p(\mathbf{s}_{k-1} \mid \mathbf{y}_{1:k-1}) \tag{1.7}$$

Here, the distributions $p(\mathbf{s}_k \mid \mathbf{y}_{1:k})$ are approximated by normal distributions with mean $\hat{\mathbf{s}}_{k|k}$ and variance $P_{k|k}$. Prior to observing the measurement $\mathbf{y}_k$, we can *predict* the unobserved state $\mathbf{s}_k$ conditioned on the prior observations $\mathbf{y}_{1:k-1}$ as

$$\begin{aligned} p(\mathbf{s}_k \mid \mathbf{y}_{1:k-1}) &\propto p(\mathbf{s}_k \mid \mathbf{s}_{k-1})p(\mathbf{s}_{k-1} \mid \mathbf{y}_{1:k-1}) \\ &= \mathcal{N}(\mathbf{s}_k \mid \hat{\mathbf{s}}_{k|k-1}, P_{k|k-1}) \end{aligned} \tag{1.8}$$

with mean $\hat{\mathbf{s}}_{k|k-1}$ and covariance $P_{k|k-1}$ given by

$$\begin{aligned} \hat{\mathbf{s}}_{k|k-1} &= \hat{\mathbf{s}}_{k-1|k-1} + \mathbf{w} \\ P_{k|k-1} &= P_{k-1|k-1} + R_k \end{aligned} \tag{1.9}$$

where the process model covariance R_k is given by equation (1.4). Using this estimate for $\mathbf{s}_k$, we linearize the measurement model to obtain a tractable linear model of the form

$$\mathbf{h}_k(\mathbf{s}_k) \approx \mathbf{h}_k(\hat{\mathbf{s}}_{k|k-1}) + (\mathbf{s}_k - \hat{\mathbf{s}}_{k|k-1}) \cdot \nabla \mathbf{h}(\hat{\mathbf{s}}_{k|k-1}) = H_k \mathbf{s}_k + \mathbf{v}_k \tag{1.10}$$

where the matrix H_k and and vector $\mathbf{v}_k$ are given by

$$\begin{aligned} H_k &= \begin{bmatrix} b\cos(\hat{\chi}_{k|k-1}) g'(\hat{\theta}_{k|k-1}) & b\sin(\hat{\chi}_{k|k-1}) g(\hat{\theta}_{k|k-1}) & 1 & 0 \\ b\sin(\hat{\chi}_{k|k-1}) g'(\hat{\theta}_{k|k-1}) & b\cos(\hat{\chi}_{k|k-1}) g(\hat{\theta}_{k|k-1}) & 0 & 1 \end{bmatrix} \\ \mathbf{v}_k &= \mathbf{h}_k(\hat{\mathbf{s}}_{k|k-1}) - H_k \hat{\mathbf{s}}_{k|k-1} \end{aligned} \tag{1.11}$$

This approach based on linearizing the nonlinear model around the current state estimate is known as the extended Kalman filter (EKF). Using the linearized measurement model, we can *update* the prior estimate $\hat{\mathbf{s}}_{k|k-1}$ on the latest observation $\mathbf{y}_k$ as

$$\begin{aligned} p(\mathbf{s}_k \mid \mathbf{y}_{1:k}) &\propto p(\mathbf{y}_k \mid \mathbf{s}_k) p(\mathbf{s}_k \mid \mathbf{y}_{1:k-1}) \\ &= \mathcal{N}(\mathbf{s}_k \mid \hat{\mathbf{s}}_{k|k}, P_{k|k}) \end{aligned} \tag{1.12}$$

with mean $\hat{\mathbf{s}}_{k|k}$ and covariance $P_{k|k}$ given by

$$\begin{aligned} \hat{\mathbf{s}}_{k|k} &= P_{k|k} \big(P_{k|k-1}^{-1} \hat{\mathbf{s}}_{k|k-1} + \sigma^{-2} H_k^\top (\mathbf{y}_k - \mathbf{v}_k) \big) \\ P_{k|k} &= \big(P_{k|k-1}^{-1} + \sigma^{-2} H_k^\top H_k \big)^{-1} \end{aligned} \tag{1.13}$$

Backward Kalman Smoothing. During the second "smoothing" step, we progress backwards through the unobserved states $\mathbf{s}_k$ from $k = N$ to 1 conditioning on all observations $\mathbf{y}_{1:N}$. In progressing from index $k+1$ to k, we use the following relationship

$$p(\mathbf{s}_k \mid \mathbf{y}_{1:N}) = p(\mathbf{s}_k \mid \mathbf{y}_{1:k}) \int \frac{p(\mathbf{s}_{k-1} \mid \mathbf{s}_k) p(\mathbf{s}_{k-1} \mid \mathbf{y}_{1:N})}{p(\mathbf{s}_{k-1} \mid \mathbf{y}_{1:k})} d\mathbf{s}_{k-1} \tag{1.14}$$

which involves the following distributions defined above

$$\begin{aligned} p(\mathbf{s}_k \mid \mathbf{y}_{1:k}) &= \mathcal{N}(\mathbf{s}_k \mid \hat{\mathbf{s}}_{k|k}, P_{k|k}) \\ p(\mathbf{s}_{k-1} \mid \mathbf{s}_k) &= \mathcal{N}(\mathbf{s}_{k-1} \mid \mathbf{s}_k + \mathbf{w}, R_k) \\ p(\mathbf{s}_{k-1} \mid \mathbf{y}_{1:k}) &= \mathcal{N}(\mathbf{s}_{k-1} \mid \hat{\mathbf{s}}_{k-1|k}, P_{k-1|k}) \end{aligned} \tag{1.15}$$

Due to the linear process model and the linearized measurement model, the posterior distribution $p(\mathbf{s}_k \mid \mathbf{y}_{1:N})$ is also normally distributed with mean $\hat{\mathbf{s}}_{k|N}$ and covariance $P_{k|N}$. Using equation (1.14), we can related these quantities for the k time step to the those of the $k+1$ time step as

$$\begin{aligned} \hat{\mathbf{s}}_{k|N} &= \hat{\mathbf{s}}_{k|k} + C_k (\hat{\mathbf{s}}_{k-1|N} - \hat{\mathbf{s}}_{k-1|k}) \\ P_{k|N} &= P_{k|k} + C_k (P_{k-1|N} - P_{k-1|k}) C_k^\top \end{aligned} \tag{1.16}$$

where $C_k = P_{k|k} P_{k-1|k}^{-1}$. The inference of hidden state variables $\mathbf{s}_{1:N}$ via Kalman filtering and smoothing depends on the ability of the linearized measurement model to accurately approximate the full nonlinear problem. This accuracy can be improved by iterative application of the the filtering and smoothing steps, in which the measurement model is linearized about the previous posterior estimates $\hat{\mathbf{s}}_{k|N}$.

Supplemental Note 2: Calibration of the simulations and pair-wise interactions between oscillators

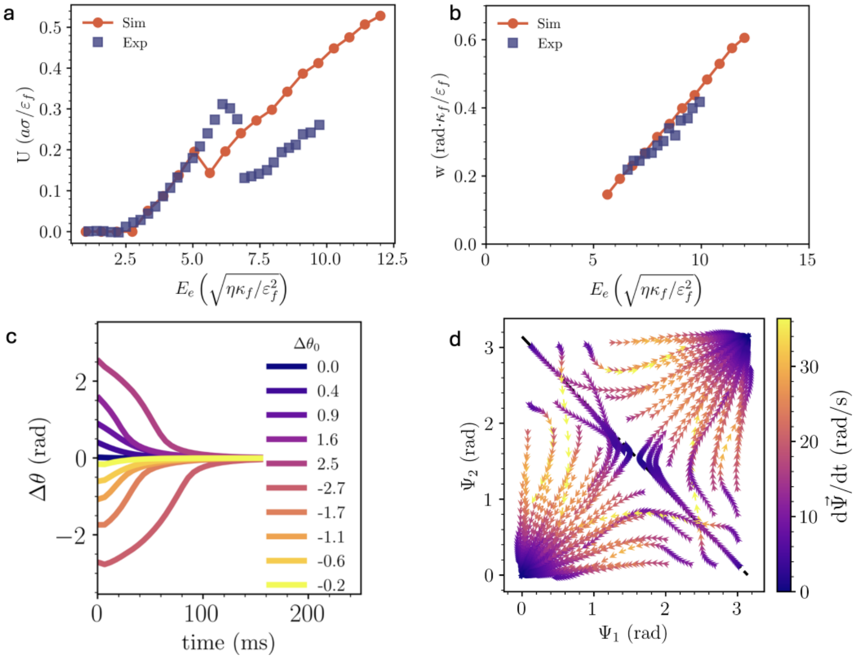

Figure S2: (a) Average speed of the oscillators as a function of the electric field in experiments and in simulations, using the Stokesian Dynamics method. The sharp decrease of the velocity shows the transition towars the oscillatory regime. The experiments in the main text were performed at $E_e = 6$ V/μm, which in dimensionless units corresponds to $10\sqrt{\eta\kappa_f/\varepsilon_f^2}$. (b)Frequency of oscillation in the particles in experiments and using the Stokesian Dynamics simulation methodology. Accounting for the conductivity gradient within the multipolar expansion approximation allows to capture quantitatively the oscillation frequency of the particles. (c) Evolution of the phase difference between two particles, the center of oscillations of which are placed at a distance d=3a. The particles are initialised with an initial phase difference, and are observed to quickly synchronise their phases, within a time in the range of 100 ms. (d) Diagram showing the evolution of the axis of oscillation between two particles for different initialisations of synchronised, not-aligned particles. The angles Ψ_1, Ψ_2 correspond to the angle between the particle oscillation axis and the line joining the center of oscillation of the particles, $\Psi \quad = \chi \qquad$, where is the angle of the vector joining the center of the two particles. In all simulations, particles are fully aligned after 200 ms. The points (Ψ_1, Ψ_2)=(0,0) and $(\Psi_1, \Psi_2)=(\pi, \pi)$ corresponds to equivalent symmetric states, where particles oscillate in the same axis. The diagram shows the two aforementioned are stable points of oscillation. Turning off dipolar interactions yields the same quantitative results.

Supplemental Note 3: Structure and ordering of the fluid phase in simulations.

The simulations exhibit the same characteristics and ordering as that observed in the experiments. As shown in Fig. S5a, the oscillators arrange in a fluid-like structure. Their phase and alignment are correlated at $\Delta\psi = \Delta\chi = 0$ and their respective equivalent points at the corners of the histogram in Fig. S5b. Fig. S5c. The simulations also show a certain tendency to increase frequency for increasing density that is less pronounced compared to the experiments. The difference between this behaviors lays in the uniform density used for initialising the simulations. In the experiments, dense fluctuations allow a larger increase of frequency of dense regions surrounded by less dense regions.

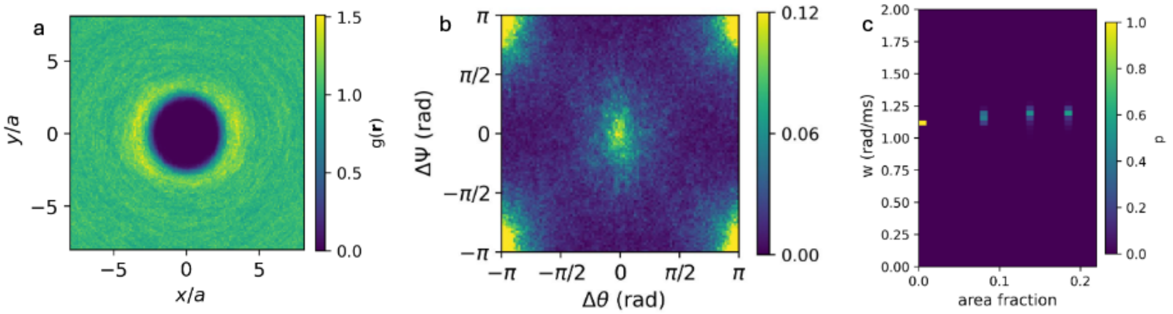

Figure S3: (a) 2D radial distribution function obtained from the simulations. (b) Histogram showing the that the phase difference $\Delta\theta$ and alignment difference $\Delta\chi$ are correlated. (c) Frequency dependence on the density. As in the experiments, the simulations show an increase in the frequency.

Supplemental Note 4: Spatial correlation length in simulations

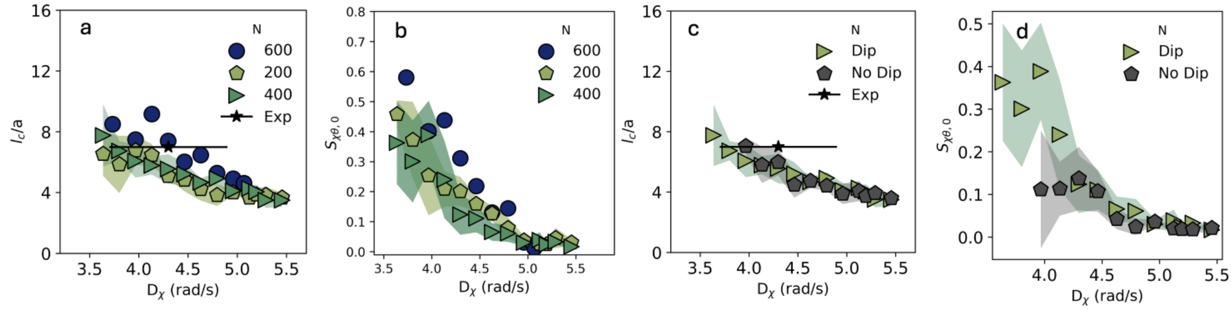

Figure S4: Characterisation of correlation length in simulations. All the simulations are performed at at an area fraction $\phi = 0.14$(a) Correlation length as a function of the diffusion coefficient for different system sizes. (b) Stabilised bulk correlation length for different system sizes (c) Comparison of simulations with and without dipolar interactions for a simulation with N=400 particles. d) Comparison bulk correlation length with and without dipolar interactions for a simulation with N=400 particles.

To characterise the phase-alignment order paramater in the simulations, the observed exponential decay is fitted to an exponential function $S_{\chi\theta} = a \exp(\quad r/l_d) + S_{\chi\theta,0}$, where l_d a spatial correlation length and $S_{\chi\theta,0}$ characterises the value at which the correlation length stabilises. If $S_{\chi\theta,0} \neq 0$ the system exhibits a certain degree of long-range ordering. In Fig. S4 we show how this spatial correlation length behaves for different sizes, and in the absence of dipolar interactions. For the simulation sizes of 200 and 400 particles, 5 repetitions of each simulation have been performed to characterize the variability of the correlation length for different random initial conditions. For the larger system size N=600 we have only performed a single simulation for each point due to its high computational cost. The shaded area for 200 and 400 particles is extracted from the standard deviation of the measurements.

The correlation lengths is always close to the experimental range within the error bars, showing a quantitative agreement for smaller diffusion coefficients. Fig. S4a shows two trends: A tendency to larger standard deviations for smaller diffusion coefficients and a tendency to decrease the correlation length with increasing diffusion coefficient. The first one is related to a higher influence of the specific spatial configuration of the oscillators for smaller diffusion coefficients. When randomly distributing the particles in the simulation box, after a transient time, the center of oscillations of each particle remains still. Hence a smaller diffusion coefficient makes the system more prone to freeze at a certain spatial configuration that yields a different correlation length. However, as noise increases, the standard deviation also decreases, meaning that the initialisation of the system becomes less significant. The value at which the exponential decay saturates is shown in Fig. S4b. The same trends are observed as in Fig. S4a, but we get additional informatio on how correlated the system is at larger distances. The results show that for diffusion coefficients $D_\chi > 4.5$ rad$/s^2$ the system is not correlated at long range. Finally, Figures S4c shows a comparison between simulations with and withoud dipolar interactions. Interestingly, the results show quantitatively the same correlation lengths, showing that the origin of this correlation length is mainly of hydrodynamic. Furthermore, S4d shows that in the absence of dipolar interactions the system exhibits less long range ordering. In the absence of both dipolar and hydrodynamic interactions the simulationr results are trivial: Since the system is not dense enough to interact through excluded volume interactions, oscillations take place independently and the fluid phase stays uncorrelated during the simulations. Taken together, this results highlight the role of hydrodynamic interactions as the main mechanism of ordering for the fluid phase.

Supplemental Note 5: Evaluation of dynamical order parameters for oscillatory modes

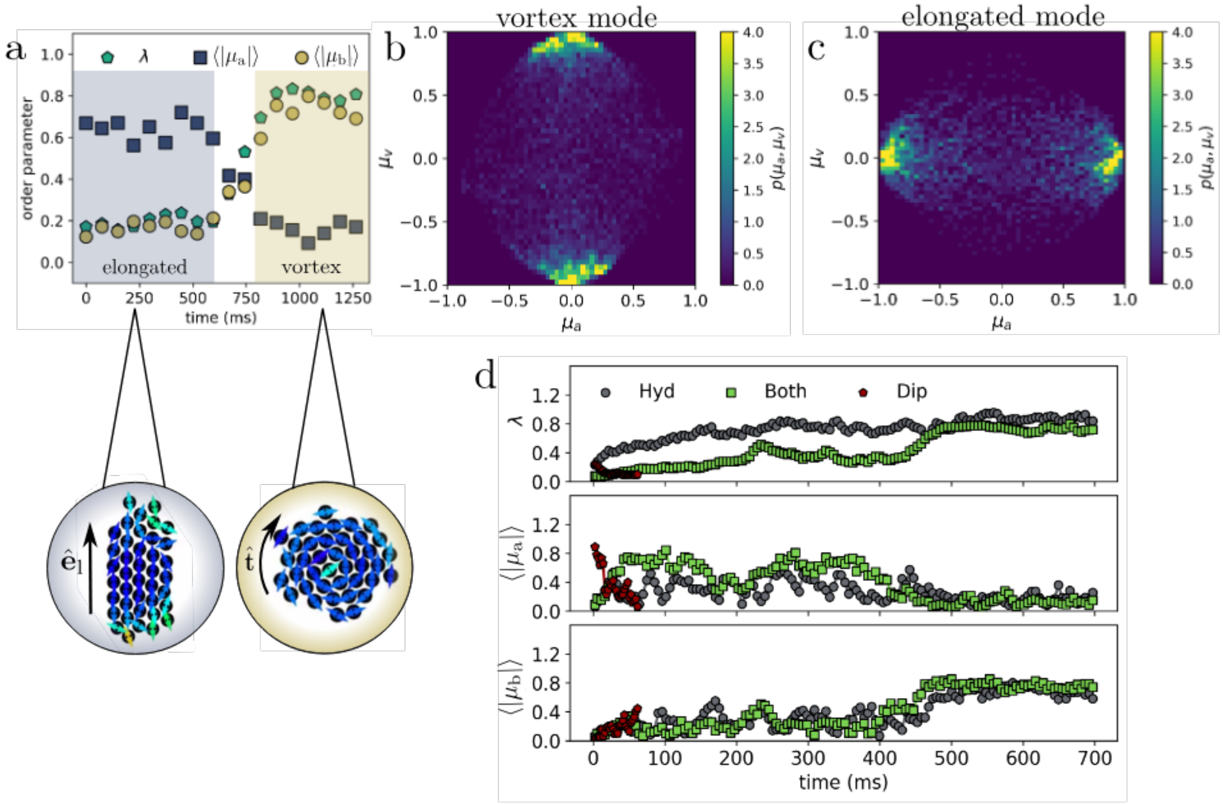

Figure S5: (a) Evolution of the averaged dynamic order parameters μ_a and μ_v. (b) 2D-histogram of μ_a *vs* μ_v during the vortex mode. The distribution shows two region of minima around $\mu_a = 0$ and $\mu_v = \pm 1$ corresponding to the clockwise and counterclockwise vortex oscillation. (c) 2D-histogram of μ_a *vs* μ_v during the vortex mode. The distribution shows two region of minima around $\mu_a = \pm 1$ and $\mu_v = \pm 0$ corresponding to oscillations in the direction of the elongation and in its opposite direction. d) Comparison of the different dynamical parameters for different combinations of the interactions as in the main figure in the text.

References

1. Zhang, Z. & Bishop, K. J. M. Synchronization and alignment of model oscillators based on Quincke rotation. *Phys Rev E* **107,** 054603 (2023).
2. Bishop, C. M. *Pattern recognition and machine learning* (Springer, 2006).
3. Kalman, R. E. A New Approach to Linear Filtering and Prediction Problems. *J Basic Eng* **382,** 35–45 (1960).
4. Rauch, H. E., Tung, F. & Striebel, C. T. Maximum likelihood estimates of linear dynamic systems. *AIAA J* **3,** 1445–1450 (1965).